Fuel 381 (2025) 133338

Contents lists available at ScienceDirect

Fuel

journal homepage: www.elsevier.com/locate/fuel

Full Length Article

Radiation modelling considering burnout-dependent properties and cellwise non-uniform particle distributions in the numerical simulation of pulverised solid fuel combustion

Hossein Askarizadeh [a,*], Stefan Pielsticker [a], Hendrik Nicolai [b], Matthias Koch [a], Reinhold Kneer [a], Christian Hasse [b], Anna Maßmeyer [a]

[a] Institute of Heat and Mass Transfer (WSA), RWTH Aachen University, Augustinerbach 6, 52056 Aachen, Germany
[b] Institute for Simulation of Reactive Thermo-Fluid Systems (STFS), Technische Universität Darmstadt, Otto-Berndt-Str. 2, 64287 Darmstadt, Germany

ARTICLE INFO

Dataset link: 10.18154/RWTH-2024-07124

Keywords:
Pulverised solid fuel combustion
Oxyfuel conditions
Gas and particle radiation
Burnout-dependent particle radiative properties
Absorption and scattering efficiencies
Weighted-scaling approach

ABSTRACT

The present study evaluates the impact of the gas and particle radiation on flame characteristics of a pulverised solid fuel using Reynolds-averaged Navier–Stokes (RANS) equations. As a reference, a pilot-scale combustor with a 60 kW_{th} flame is used. The burner is fed with pulverised (10 – 180 μm) Rhenish lignite particles under oxyfuel conditions (25/75 vol % O_2/CO_2). CFD simulations are carried out using Ansys Fluent equipped with user-defined functions (UDFs), e.g., for gas and particle radiative properties and kinetic models (devolatilisation and char conversion) adapted for oxyfuel conditions. Particular focus is placed on evaluating detailed modelling of the particle radiative properties, which are determined with the aid of Mie theory and taken into account in the simulations via UDFs as tabulated data. For this purpose, simulation results for the reference case with constant particle radiative properties (a common assumption in the relevant literature) are compared to those obtained with burnout-dependent particle radiative properties (determined using the Mie theory — Mie case) as well as to those obtained considering the effect of cellwise non-uniform distributed particles on the burnout-dependent particle radiative properties (within the framework of a recently proposed weighted-scaling approach — WSA case). Simulation results show that the role of particle radiation is more pronounced in the near-burner region, such that comparisons of the predicted temperatures in different models signify high local temperature differences. The importance of particle radiation reduces with the axial distance from the burner until the differences in the predicted temperatures in all three cases become negligible. In the near-burner region, predictions of the reference case on the particle radiative fluxes are much smaller than those of the Mie and WSA case. These differences lead to high local temperature differences, especially where strong temperature gradients exist.

1. Introduction

Combustion of solid fuels is still responsible for a significant share of anthropogenic CO_2 emissions [1]. Additional capture and geological storage of CO_2 (CCS) can contribute to a considerable reduction of CO_2 emissions. One promising way to facilitate CCS is combustion in an oxyfuel atmosphere (mixture of O_2/CO_2) instead of air. However, efficient combustion of solid fuels under oxyfuel conditions requires a thorough characterisation of the combustion process. Due to the complex and highly non-linear nature of phenomena occurring during the combustion of solid fuels, a combination of experimental and numerical methods is necessary to fully characterise oxyfuel flames.

The subprocesses involved in the combustion of pulverised solid fuels can be clustered into the following categories: chemical reactions, turbulence-chemistry interaction, gas radiation, and particle-radiation interaction [2]. An important aspect to be considered in numerical simulations is that these subprocesses are strongly influenced by the high CO_2 concentrations in an oxyfuel atmosphere in comparison to air characterised by high N_2 concentrations. This necessitates a comprehensive re-evaluation of the existing modelling approaches that have been developed over the last decades for solid fuel combustion in air atmospheres.

One of the important aspects in this regard is the reaction kinetics of the solid phase that significantly influences the flame shape. Using a new seamless model (CRECK-S) [3,4] for the description of the entire conversion process together with a flamelet-based description of the gas phase, Nicolai [5] and Nicolai et al. [6,7] showed that if the kinetic

* Corresponding author.
E-mail address: askarizadeh@wsa.rwth-aachen.de (H. Askarizadeh).

https://doi.org/10.1016/j.fuel.2024.133338
Received 22 November 2023; Received in revised form 30 July 2024; Accepted 30 September 2024
Available online 17 October 2024

parameters of the reaction of the solid phase are accurately determined for the simple models, e.g., the single first-order reaction (SFOR) model proposed by Badzioch and Hawksley [8] for devolatilisation and the Baum and Street model [9,10] for char conversion, important characteristics of the flame such as temperatures and conversion rates can be correctly reflected. Hence, in this study, the SFOR and the Baum and Street model for char conversion are adopted for oxyfuel conditions and applied as user-defined functions in the simulations.

Another important modelling aspect concerns gas and particle radiation. Gas radiative property models in oxyfuel atmospheres have been extensively studied in the related literature [11,12]. In general, the most accurate gas radiative property models are – in order of decreasing complexity – the line-by-line, statistical narrow band, wide band, and global models [13]. Among others, global models, such as the weighted-sum-of-grey-gases (WSGG) model [14], directly calculate the total radiative fluxes – the quantity of interest in the simulation of combustion chambers – using spectrally integrated radiative properties and are thus widely used for simulation purposes.

In contrast to gas radiation, only a few studies have taken into account detailed modelling of particle radiation in simulations of pulverised solid fuels. Some studies, e.g., Nikolopoulos et al. [15], have neglected the impact of particle radiation and the majority of relevant studies relied on the empirical constant of particle emissivity of ϵ_p = 0.7−0.9 and a constant particle scattering factor f_p = 0.6 or 0.9 [16–18]. However, evidence on the variation of the complex index of refraction due to unburnt char and also the sudden decrease in the absorption efficiency near burnout [19–21] signifies the possible important influence of particle radiative properties on flame characteristics. In this regard, linearly varying conversion-dependent particle radiative properties, including the degree of conversion, were considered in the CFD simulation of pulverised coal combustion [22,23]. The linear variation was used to mimic the effect of fly ash (strongly scattering) and char particles (strongly absorbing) on the particle radiative properties. A more accurate approach than a linear variation was developed by Guo et al. [24] based on the concept of a weighted sum of four grey particles and a spectrum k-distribution, which can be combined with a non-grey WSGG model without increasing computational complexity.

Concerning the assessment of radiation modelling in swirling flames under oxyfuel conditions, a 2D numerical study by Guo et al. [25] on the IFRF's swirling oxyfuel flame of pulverised coal revealed that both gas and particle radiation affect flame temperature and shape. In addition, neglecting radiation led to an increase in the flame temperature up to 300 K. However, assessment of the *level of detail* in radiation modelling of the particle phase and using 3D simulation of swirling pulverised solid fuel flames does not exist in the related literature to the best of authors knowledge.

To evaluate the needed level of detail in radiation modelling, a 3D RANS simulation tool developed in Ansys Fluent [26,27] is used in this study. The numerical tool is equipped with user-defined functions (UDFs) adapting (1) the kinetic models (devolatilisation and char conversion) for oxyfuel conditions, (2) the gas radiative properties model by implementing a modified WSGGM suitable for oxyfuel combustion proposed by Bordbar et al. [11], and (3) inclusion of burnout-dependent particle radiative properties for the calculation of absorption and scattering coefficients. In this regard, the sensitivity of the simulation results on the particle radiative properties under oxyfuel conditions is studied. In addition, a recently developed weighted-scaling approach [28] is considered, which accounts for the cellwise non-uniform particle distribution effects on the burnout-dependent particle radiative properties.

In the following, the experimental reference case used for the evaluation of radiation modelling is introduced in Section 2, followed by the description of the numerical approach (Section 3) and the calculation method for determining particle radiative properties using Mie theory in Section 4.

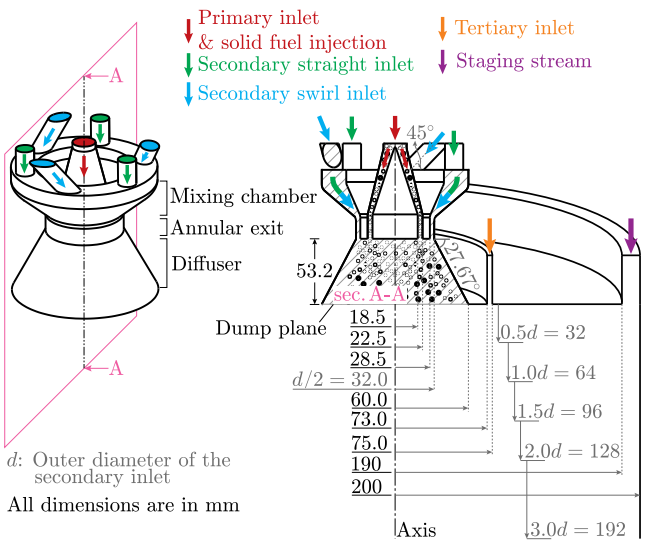

Fig. 1. (left) Burner head with primary and secondary inlets; and (right) cross-sectional view of the inlets supplemented by the dimensions of the burner and combustion chamber. The primary inlet is an annular tube. The secondary inlet consists of 3 straight and 3 tilted inlets followed by a small mixing chamber. The inlets are discharged into this mixing chamber, after which the mixed secondary flow enters the chamber through the diffuser. The exemplary axial levels specified by d below the dump plane are the levels for which measurement data on axial and tangential particle velocity components are available. Other measurement levels are $4.0d$ = 256 mm, $5.0d$ = 320 mm, and $6.0d$ = 384 mm. For particle temperature, the measurement levels are 100 mm = $1.5625d$, 200 mm = $3.125d$, and 300 mm = $4.6875d$. (For interpretation of the references to colour in this figure legend, the reader is referred to the web version of this article.)

2. Reference case

The 60 kW_{th} oxyfuel flame called Oxy25, i.e., under oxyfuel conditions of 25 vol% O_2 and 75 vol% CO_2, has been chosen from the investigated flames by Zabrodiec et al. [29]. The schematic view of the burner and combustion chamber is presented in Fig. 1.

The burner has two inlets: (1) a primary inlet consisting of an annular tube carrying the pulverised solid fuel particles through the oxidiser, and (2) a secondary inlet consisting of 3 straight and 3 inclined channels, both carrying oxidant and mix in a small mixing chamber. The volume flow rates of the straight and inclined channels control the strength of the swirling flow. A third and a fourth annular orifice – called the tertiary inlet and staging stream, respectively – provide additional oxidiser to the chamber. The axial traversability of the burner enables an investigation of almost the entire flame by measuring at different distances below the dump plane (diffuser outlet). Three observation ports at a fixed level permit optical access and probe-based measurements.

The fuel is Rhenish lignite with proximate, ultimate and particle size analysis given by Zabrodiec et al. [29] and presented in Table 1. The operating conditions for the Oxy25 flame are provided in Table 2. The chamber wall was heated electrically and constantly to ≈ 900 °C during the experiments to have a defined boundary condition for characterising the flame [29].

3. Numerical approach

Numerical simulation of the reference case is carried out using Ansys Fluent 17.1. Continuous and discrete phases are solved in a coupled manner under the boundary and operating conditions given in Table 2. The *coupled* scheme (pressure-based coupled solver) for velocity–pressure is used with a pseudo-transient solution strategy, which adds an unsteady term to the steady equations to improve stability and convergence. Additional transport equations for species and the

Table 1
Physical and chemical properties of Rhenish lignite (RBK) according to ultimate, proximate, and microscopic particle size analysis given by Zabrodiec et al. [29].

Component			RBK
C	[wt%]	daf[b]	69.05
H	[wt%]	daf[b]	4.83
N	[wt%]	daf[b]	0.69
S	[wt%]	daf[b]	0.30
O[a]	[wt%]	daf[b]	25.13
Ash	[wt%]	ar[c]	5.44
Water	[wt%]	ar[c]	12.15
Volatiles	[wt%]	ar[c]	42.42
Char[a]	[wt%]	ar[c]	39.99
Higher heating value	[MJ/kg]	ar[c]	22.153
$d_{p,10}$	[µm]		5.61
$d_{p,50}$	[µm]		29.67
$d_{p,90}$	[µm]		132.62

[a] From difference.
[b] Reference state: dry, ash-free.
[c] ar: as received.

Table 2
Operating conditions of the Oxy25 flame taken from Zabrodiec et al. [29].

Primary inlet		
Coal mass flow rate	[kg/h]	9.8
Volume flow rate[a]	[m^3/h]	9.4
O_2/CO_2 fraction	[vol %]/[vol %]	20.2/79.8
Temperature	[°C]	25
Secondary inlet		
Volume flow rate[a]	[m^3/h]	23.8
O_2/CO_2 fraction	[vol %]/[vol %]	25/75
Temperature	[°C]	40
Swirl number	[−]	0.95[b]
Tertiary inlet		
Volume flow rate[a]	[m^3/h]	4.2
O_2/CO_2 fraction	[vol %]/[vol %]	25/75
Temperature	[°C]	25
Staging stream		
Volume flow rate[a]	[m^3/h]	22.2
O_2/CO_2 fraction	[vol %]/[vol %]	25/75
Temperature	[°C]	900

[a] STP: standard temperature 0 °C and pressure 1.013 bar.
[b] Estimated using the geometrical parameters of the burner [30].

energy conservation equation are solved [31,32]. Below, the numerical modelling is first described, before Section 4 explicitly focuses on the radiation modelling.

3.1. Continuous-phase modelling

For the continuous phase, appropriate turbulence, reaction kinetics, and turbulence-chemistry interaction modelling are of significant importance in obtaining the characteristics of the flame. A detailed overview of the governing equations needed to be solved here is given in Askarizadeh et al. [32].

3.1.1. Turbulence

The realisable variant of the k-ε model family was chosen to simulate the swirling turbulent flow in the combustion chamber. The reason for choosing this model was an extensive preliminary study carried out using realisable and renormalisation group (RNG) k-ε models as well as the Reynolds stress model (RSM), indicating the suitability of a realisable model. Note, for RANS simulations of turbulent swirling flows, only these three models should be used, since the nature of swirling flows has only been considered in these models [31]. The RSM is also suitable, however, it is recommended for highly swirling flows.

3.1.2. Continuous-phase chemistry

A reaction mechanism in the gas phase composed of a system of two main reactions is considered, whereby the volatile gases are modelled as a single postulated substance [33,34]:

$$C_xH_yO_lN_mS_n + 0.882\,O_2 \rightarrow 0.99\,CO + 1.39\,H_2O + 0.0143\,N_2 + 0.0054\,SO_2$$

with $A = 2.119 \cdot 10^{11}\ s^{-1}$ and $E_a = 2.027 \cdot 10^5\ J/mol$

and

$$CO + 0.5\,O_2 \rightarrow CO_2$$

with $A = 2.239 \cdot 10^{12}\ s^{-1}$ and $E_a = 1.7 \cdot 10^5\ J/mol$.

The coal calculator embedded in Fluent was used to determine the volatile composition as $C_{0.99}H_{2.79}O_{0.91}N_{0.0287}S_{0.0054}$. The rate coefficients are also given by the coal calculator [31].

The gas mixture properties are calculated using the ideal gas mixing law embedded in Fluent. For each gas species (Y_i) participating in the chemical reactions, viscosity and thermal conductivity are considered as fourth-order temperature-dependent polynomials available in the Fluent database. A transport equation is solved for each species in the gas mixture and the solution of these equations needs a closure for the chemical source terms. This is treated by the turbulence-chemistry interaction modelling.

3.1.3. Turbulence-chemistry interaction

The turbulence-chemistry interaction is modelled using the eddy dissipation concept (EDC) that takes into account chemical mechanisms in turbulent flows, assuming the occurrence of species reactions in the fine structures of turbulence [31,35].

3.2. Particle-phase modelling

3.2.1. Particle dynamics

Combusting particles are assumed spherical and are tracked in the chamber using a Lagrangian reference frame [31]. The momentum balance is used to calculate particle trajectories. Since the particle volume fraction is high in the near burner region (specified in a prior study [36]), a two-way coupling approach is applied to take into account turbulence modulation of the continuous phase caused by the discrete phase according to Al Taweel and Landau [37]. In addition, drag, gravitational, and thermophoretic forces are taken into account according to previous studies [32,38,39] as being important to determine the movement of particles in the chamber.

The momentum balance of the particle is integrated over a length scale $l = 5 \cdot 10^{-4}$ m and for a maximum number of steps $n_{steps} = 5 \cdot 10^4$. The stochastic tracking is carried out using the discrete random walk model to account for the effect of turbulent velocity fluctuations on the particle trajectories. The number of 50 tries was determined by keeping the time scale constant of the model equal to 0.15 [31] and repeating the simulations by increasing the number of tries until no significant changes were observed in the simulation results [40].

3.2.2. Particle heat transfer

For the calculation of heat transfer from/to a particle during the combustion process in the chamber, the following energy balance is solved:

$$m_p c_p \frac{dT_p}{dt} = hA_p\left(T_\infty - T_p\right) - f_h \frac{dm_p}{dt} H_{reac} + \epsilon_p A_p \sigma \left(\theta_p^4 - T_p^4\right) \quad (1a)$$

$$\theta_p = \left(\frac{G}{4\sigma}\right)^{\frac{1}{4}}, \quad (1b)$$

$$G = \int_0^{4\pi} I_s d\Omega, \quad (1c)$$

In Eqs. (1a), m_p indicates the particle mass, c_p specific heat capacity, T_p particle temperature, t time, h convective heat transfer coefficient, A_p particle surface, T_∞ gas local temperature, ϵ_p particle emissivity,

σ Stefan–Boltzmann constant, and I_s is the incident radiation. The heat released from the particle is denoted by H_{reac} and the coefficient f_h signifies that part of the heat released is absorbed directly by the particle and the rest is released in the gas phase [31,41]. In this study, CO is considered as the only char burnout product.

Calculation of the convective heat transfer coefficient h is carried out according to Frössling [42] and Ranz [43] as follows:

$$\mathrm{Nu}_d = \frac{h\, d_\mathrm{p}}{k} = 2 + 0.6\, \mathrm{Re}_{d_\mathrm{p}}^{\frac{1}{2}}\, \mathrm{Pr}^{\frac{1}{3}}, \tag{2a}$$

$$\mathrm{Pr} = \frac{c_{p,\mathrm{g}}\, \mu}{k}, \tag{2b}$$

$$\mathrm{Re}_{d_\mathrm{p}} = \frac{\rho\, d_\mathrm{p} \left|\vec{v}_\mathrm{p} - \vec{v}_\mathrm{g}\right|}{\mu}, \tag{2c}$$

where Nu_d is the particle Nusselt number, d_p particle diameter, Re_d particle Reynolds number, Pr Prandtl number, and $\vec{v}_\mathrm{p}$ the particle velocity. The specific heat capacity, thermal conductivity, dynamic viscosity, density and velocity of the gas mixture are denoted by $c_{p,\mathrm{g}}$, k, μ, ρ, $\vec{v}_\mathrm{g}$, respectively.

The calculated heat transfer to/from a particle using Eq. (2a) is considered as a heat sink/source in the energy balance of the continuous phase.

3.2.3. Particle reaction kinetics

Accurate modelling of the particle reaction kinetics is of significant importance in characterising the flame. Reactive solid fuel particles undergo two main subprocesses in a high-temperature medium, i.e., devolatilisation and char conversion. The kinetic parameters of these subprocesses are affected under oxyfuel conditions. According to Nicolai [5] and Nicolai et al. [6,7], using simplified models for devolatilisation and char conversion can deliver good agreement if the kinetic parameters are accurately determined for these simple models. In this regard, the single first-order reaction (SFOR) model [8] for devolatilisation and the Baum and Street model [9,10] for char conversion are used with the kinetic parameters applied by Nicolai et al. [39].

Particle devolatilisation

In the SFOR model [8], the devolatilisation rate is calculated as follows:

$$\begin{aligned} &\frac{\mathrm{d}m_\mathrm{p}(t)}{\mathrm{d}t} = k\left[m_\mathrm{p} - \left(1 - f_{v,0}\right) m_{\mathrm{p},0}\right] \quad \text{and} \quad k = A e^{-E/RT_\mathrm{p}}, \\ &A = 29\,058\ \mathrm{s}^{-1} \quad \text{and} \quad E = 42.879\ \mathrm{kJ/mol} \end{aligned} \tag{3}$$

where $f_{v,0}$ is the mass fraction of volatiles initially present in the particle, R is the universal gas constant and $m_{\mathrm{p},0}$ is the initial particle mass.

Char conversion

In the Baum and Street model [9,10], the char conversion rate is limited either by particle reaction kinetics or diffusion in the particle. This is done by weighting a kinetic reaction rate $\mathcal{R}_k$ and an effective diffusion rate D_0 resulting in the following char conversion rate:

$$\begin{aligned} &\frac{\mathrm{d}m_\mathrm{p}(t)}{\mathrm{d}t} = -A_\mathrm{p} \frac{\rho R T_\infty Y_\mathrm{i}}{M_{w,\mathrm{i}}} \frac{D_0 \mathcal{R}_k}{D_0 + \mathcal{R}_k} \\ &D_0 = C_1 \frac{\left[\left(T_\mathrm{p} + T_\infty\right)/2\right]^{\frac{3}{4}}}{d_\mathrm{p}} \quad \text{and} \quad \mathcal{R}_k = C_2 e^{-E/RT_\mathrm{p}}, \end{aligned} \tag{4}$$

where, coefficients C_1 and C_2 depend on the temperature and conversion agents, which are oxygen, carbon dioxide and water vapour. The numerical values for C_1 and C_2 together with the activation energy of the reactions are given in Table 3.

Table 3
Activation energy and rate constants of conversion reactions in low-temperature (LT) $T \leq 950\,^\circ\mathrm{C}$ and high-temperature (HT) $T > 950\,^\circ\mathrm{C}$ ranges [33,39].

Oxidiser	O_2 [39]	CO_2 [33]	H_2O [33]
C_1 [s/K$^{0.75}$]	$7.430 \cdot 10^{-13}$	$1.0 \cdot 10^{-10}$	$2.84 \cdot 10^{-12}$
C_2 [s/m]	188.6	$1.35 \cdot 10^{-4}$ [a] $6.35 \cdot 10^{-3}$ [b]	$1.92 \cdot 10^{-3}$
E [J/mol]	$1.286 \cdot 10^{5}$	$1.35 \cdot 10^{5}$ [a] $1.62 \cdot 10^{5}$ [b]	$1.47 \cdot 10^{5}$

[a] Low temperature.
[b] High temperature.

4. Radiation modelling

High temperatures in the combustion chamber signify the dominant role of radiation among other mechanisms of heat transfer in the chamber. Hence, correct modelling of radiation is of significant importance for the characterisation of the flame structure.

The radiation transfer equation that accounts for gas radiation and particle radiation interactions can be expressed for the discrete ordinate model as follows [31]:

$$\begin{aligned} \frac{\mathrm{d}I\left(\vec{r},\vec{s}\right)}{\mathrm{d}s} = &\underbrace{\kappa_\mathrm{g} n^2 \frac{\sigma T^4}{\pi}}_{\text{gas emission}} + \underbrace{E_\mathrm{p}}_{\text{particle emission}} - \overbrace{\underbrace{\left(\kappa_\mathrm{g} + \kappa_\mathrm{p} + \sigma_\mathrm{p}\right) I\left(\vec{r},\vec{s}\right)}_{\text{radiation attenuation}}}^{\text{attenuation coefficient}} \\ &+ \underbrace{\frac{\sigma_\mathrm{p}}{4\pi} \int_0^{4\pi} I\left(\vec{r},\vec{s}\prime\right) \Phi\left(\vec{s},\vec{s}\prime\right) \mathrm{d}\Omega}_{\text{inscattering}}. \end{aligned} \tag{5}$$

Eq. (5) describes the change in radiation intensity I along the infinitesimal path length $\mathrm{d}s$ in the direction of the solid angle $\vec{r}$. The first term on the right-hand side describes the increase in the intensity due to gas emission, with n as the refractive index of the gas and κ_g as the gas absorption coefficient. Increase in the radiation intensity due to particle emission E_p, and its calculation are explained in detail in Section 4.2. The third term on the right-hand side accounts for the intensity loss due to gas absorption, particle absorption and outscattering. Particle absorption and scattering coefficients (κ_p and σ_p) control the amount of absorbed and outscattered radiation by particles. The last term considers the intensity increase due to inscattering. Gas scattering is considered to be negligible [23,31], thus, the scattering coefficient and scattering phase function of the particles determine the inscattered radiation. In addition, Φ and Ω indicate the phase function and the solid angle, respectively. The scattering phase function Φ is modelled by an anisotropic Mie-scattering phase function, which is approximated by a finite series of Legendre polynomials [44,45].

In this study, the discrete ordinate method (DOM) is used to solve the radiation transfer equation as a field equation in each direction $\vec{s}$ (see Eq. (5)). In contrast to the P1 model, the DOM does not have any limitation regarding optical thicknesses and is superior when solving the radiation transfer equation in strongly forward scattering media [46]. Based on a verification study, the radiation transfer equation is solved every 10 iterations of the gas phase momentum and energy equations. The verification study was carried out with 5, 10, 20, 30 iterations. Reducing this number increases the computational costs and increasing this number to 20 and 30 did not result in a convergent solution of the reference case considered in this study. For the discretisation, each octant is divided into 36 solid angles following Gronarz [21]. The emissivity of the burner and the chamber wall are taken from Toporov et al. [33]. The burner port at the top of the chamber is made of ceramic materials with an emissivity of $\epsilon_\mathrm{b} = 0.3$ and the emissivity of the chamber wall is set to $\epsilon_\mathrm{w} = 0.7$.

4.1. Gas radiative properties

The wavelength dependency of the gas radiative properties under oxyfuel conditions is approximated by a modified weighted-sum-of-grey-gases (WSGG) model proposed by Bordbar et al. [11], which has shown good accuracy in the simulation of the reference case in this study [39]. This model can be expressed as follows:

$$\varepsilon = \sum_{i=0}^{N_g} a_i \left[1 - \exp\left[-K_i P_t \left(Y_{CO_2} + Y_{H_2O}\right) L\right]\right] \tag{6a}$$

$$a_i = \sum_{i=0}^{N_g} b_{i,j} T_r^j, \quad b_{i,j} = \sum_{k=0}^{N_g} C_{i,j,k} M_r^k, \quad K_i = \sum_{k=0}^{N_g} d_{i,k} M_r^k. \tag{6b}$$

where N_g is the number of grey gases (equal to 4), a the weighting factors, K the absorption coefficients correspond to the grey gases, P_t the total pressure of the mixture, $M_r = Y_{H_2O}/Y_{CO_2}$ the ratio of the molar fractions, L the path length, $T_r = T/T_{ref}$ the normalised temperature where T_{ref} has been selected as 1200 K [11], $b_{i,j}$ is a polynomial function of the ratio of the molar fractions, and $C_{i,j,k}$ and $d_{i,k}$ are the model constants given in Bordbar et al. [11]. Eqs. (6a) and (6a) reveal that the absorption coefficients are a direct function of gas temperature T and molar fractions of H_2O and CO_2.

4.2. Particulate effects

Particulate effects on the radiation heat transfer are taken into account through emission, scattering and absorption by particles. The equivalent emission of the particles is represented by E_p in Eq. (5), which can be expressed as follows:

$$E_p = \lim_{V \longrightarrow 0} \sum_{n=0}^{N} \varepsilon_{pn} A_{pn} \cdot \frac{\sigma T_{pn}^4}{\pi V}, \quad A_{pn} = \frac{\pi d_{pn}^2}{4}, \tag{7}$$

where the summation is over n particles in volume V and ε_{pn}, A_{pn}, d_{pn} and T_{pn} are the emissivity, projected area, diameter, and temperature of particle n, respectively.

The particle absorption κ_p and scattering σ_p coefficients in Eq. (5) are calculated as follows [25]:

$$\kappa_p = \lim_{V \longrightarrow 0} \sum_{n=1}^{N} Q_{abs,pn} \cdot \frac{A_{pn}}{V}, \quad \varepsilon_{pn} = Q_{abs,pn} \tag{8}$$

$$\sigma_p = \lim_{V \longrightarrow 0} \sum_{n=1}^{N} \left(1 - f_{pn}\right)\left(1 - \varepsilon_{pn}\right) \frac{A_{pn}}{V}, \tag{9}$$

$$\sigma_p = \lim_{V \longrightarrow 0} \sum_{n=1}^{N} Q_{sca,pn} \frac{A_{pn}}{V}, \tag{10}$$

where f_{pn} is the scattering factor of the nth particle and $Q_{abs,pn}$ and $Q_{sca,pn}$ are the absorption and scattering efficiencies of the nth particle, respectively.

4.2.1. Particle absorption and scattering efficiencies

In general, absorption and scattering efficiencies depend on wavelength, particle size and internal structure described by the index of refraction of the corresponding material. For the calculation, the Maxwell equations [47] are solved. For complex, arbitrarily shaped particles, typically, numerical methods, e.g., the discrete dipole approximation [48] or semi-analytical methods such as the T-Matrix method [49] are used. However, for almost spherical coal and ash particles, it is sufficient to use the Mie theory [50]. The Mie theory is an analytical solution of the Maxwell equations for a spherical and homogeneous particle and its validity for coal and ash particles has been verified by Gronarz et al. [51,52]. Accordingly, the index of refraction of coal and ash represents the material's property.

In this study, the measured data by Manickavasagam and Menguc [53] are used for the index of refraction of coal and the measured data by Goodwin and Mitchner [54] for that of ash. This, in combination with the ratio of particle perimeter and incident wavelength, is used as input for the Mie theory. Then, the Mie theory gives a solution for the Maxwell equations, where the solution consists of a series of spherical harmonics with corresponding coefficients. These coefficients are finally used to calculate the absorption and scattering efficiencies. A detailed description has been given by Bohren and Huffman [55]. In this study, calculations of the absorption and scattering efficiencies are based on the implementation by Mätzler [56]. To efficiently consider the wavelength dependency, Planck mean values are calculated utilising the following equation:

$$\overline{Q}_i = \frac{\int_\lambda Q_{\lambda,i} \cdot I_B(T_P) d\lambda}{\int_\lambda I_B(T_P) d\lambda}. \tag{11}$$

Where $I_B(T_P)$ is the temperature-dependent black body intensity. As the calculation of the spherical harmonics and the averaging process is computationally too expensive for on-the-fly CFD coupling, a pre-calculated database is created.

Accordingly, a variation of the absorption and scattering efficiencies for char (top row) and for ash (bottom row) particles over a temperature range of $T_p = 293.15 - 3000\,K$ and a diameter range of $d_p = 5 - 500\,\mu m$ is provided in Fig. 2. These are calculated using Mie theory over a wavelength range of $\lambda = 0.025 - 20\,\mu m$, where the variation of the particle absorption and scattering efficiencies is significant. The calculated efficiencies are then implemented as tabulated data and are interpolated for the current char and ash particle diameters and temperatures. The results are then combined via the burnout parameter β as follows:

$$Q_{abs} = \beta \cdot Q_{abs,char} + (1 - \beta) \cdot Q_{abs,ash}, \tag{12a}$$

$$Q_{sca} = \beta \cdot Q_{sca,char} + (1 - \beta) \cdot Q_{sca,ash}, \tag{12b}$$

$$\beta = \frac{m_{p,char}}{m_{p,0}}. \tag{12c}$$

The linear combination of efficiencies is an approximation to consider ash as well as char radiation properties. Applying other scenarios for the combination of these properties [57] can be done in the implemented UDF, which will be made accessible in software publication through the RWTH library under the DOI: 10.18154/RWTH-2024-05749 (see also Appendix).

4.2.2. Particle cloud effect with the weighted-scaling approach (WSA)

In the solution of the radiative transfer equation, applying Eqs. (8) and (10) yields an effective absorption and scattering coefficient, representing the absorption and scattering properties of the particles within a cell simultaneously. However, Koch et al. [28] discovered that this approach is only suitable for a perfectly uniform distribution of the particles within the mesh cells and when multiple scattering by the particles is negligible. To account for the effects of the non-uniform distribution of the particles in a mesh cell and to consider multiple scattering, Koch et al. [28] developed a weighted-scaling approach (WSA), which considers these effects by multiplying the scattering and absorption coefficient with a weighting factor W_p. This weighting factor W_p depends on the mean diameter of the particles in a cell and also on the mean absorption efficiency. Typical values of W_p lie in a range of 0.5 – 0.75 [28]. For more information on the derivation of these factors, see Koch et al. [28]. The inclusion of W_p in Eqs. (8) and (10) is as follows:

$$\kappa_{p,WSA} = \lim_{V \longrightarrow 0} \sum_{n=1}^{N} Q_{abs,pn} \frac{A_{pn}}{V} W_{pn}, \tag{13a}$$

$$\sigma_{p,WSA} = \lim_{V \longrightarrow 0} \sum_{n=1}^{N} Q_{sca,pn} \frac{A_{pn}}{V} W_{pn}. \tag{13b}$$

WSA leads to strong deviations in certain variables, especially in the absorption and scattering coefficients (in some cases 30% [28]). The question is how this affects the overall simulation accuracy, especially the temperature, which will be addressed in Section 5.

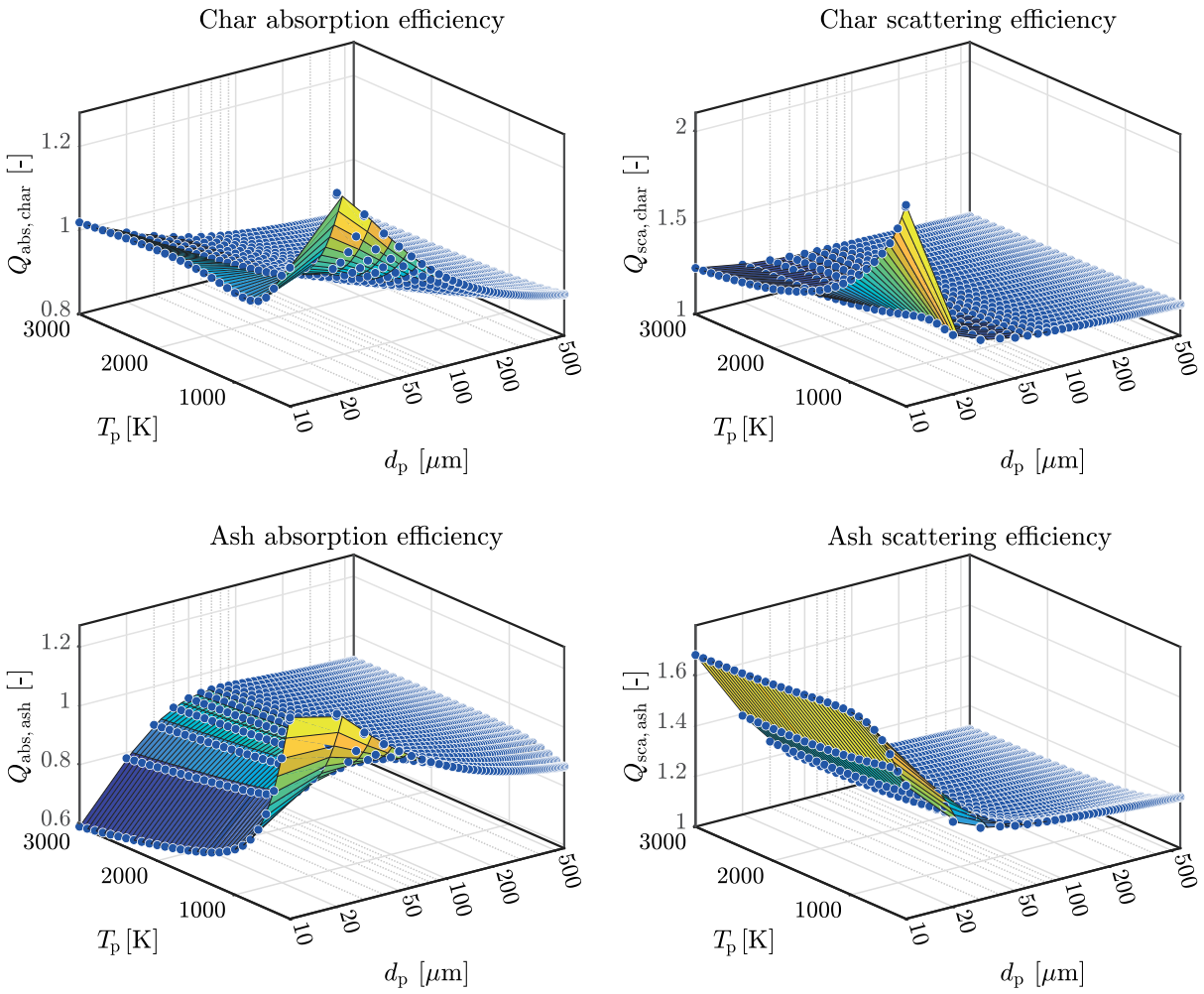

Fig. 2. Dependency of char (top row) and ash (bottom row) particle absorption (left) and scattering (right) efficiencies on particle diameter and temperature.

4.2.3. Implementation of particle absorption and scattering efficiencies

In Fluent, there are no material properties for burning particles that can be directly considered as particle absorption and scattering efficiencies. In the relevant literature, particle emissivity, ϵ_p, is assumed to be equal to the absorption efficiency, $Q_{abs,p}$ [21,25,39]. However, the inclusion of the scattering efficiency $Q_{sca,p}$ in the calculations of the scattering coefficient through Eq. (9) is not straightforward in Fluent.

In general, there are two direct possibilities to include $Q_{sca,p}$ via a UDF in Fluent: (1) through the scattering factor f_p, and (2) through defining source terms for the gas phase. Regarding the first option, in the relevant literature, e.g., Guo et al. [25], Eq. (10) is used instead of Eq. (9). This means that the following expression must be employed to determine f_p from the absorption and scattering efficiencies:

$$f_p = 1 - \frac{Q_{sca,p}}{1 - Q_{abs,p}}. \tag{14}$$

This must be done through a UDF using the module *DEFINE_DPM_PROPERTY*. However, since the value of $Q_{abs,p}$ is in most cases close to 1, Eq. (14) leads to both negative and positive values for f_p around four orders of magnitude higher than a constant value of, e.g., f_p = 0.9, which is usually used in the literature. This is a very important point, since such high values for f_p, depending on whether $Q_{abs,p}$ is larger/smaller than 1, can lead to unphysical negative scattering coefficients.

The other possible way to include $Q_{abs,p}$ and $Q_{sca,p}$ in the calculation of the absorption and scattering coefficients in Fluent is through the gas phase using the module named *DEFINE_DOM_SOURCE* or *DEFINE_DPM_SOURCE*. In this study, the module *DEFINE_DPM_SOURCE* along with the macros *C_DPMS_SCAT*, *C_DPMS_ABS*, and *C_DPMS_EMISS* is used to calculate the absorption and scattering coefficients. In this way, the absorption and scattering efficiencies, which are interpolated using the particle diameter and temperature from Fig. 2, can be used directly to calculate the absorption and scattering coefficients, so that no negative and unphysical values can result for these coefficients.

5. Results and discussions

5.1. Grid study

Due to the rotationally symmetric geometry of the combustion chamber (see Fig. 1), a quarter of it is considered for the numerical simulations. For the geometry considered, a structured mesh is generated (shown in Fig. 3) with high orthogonal quality (minimum orthogonality of 0.631 and an average of 0.987 out of 1).

The eligibility of the applied grid in the numerical simulations has recently been shown in another work of the authors [32], indicating that a grid with 744,495 cells is sufficiently fine to capture the flame characteristics investigated here by comparing the results to a finer grid with 3,309,960 cells.

5.1.1. Validation: particle velocity components and particle temperature

Particle velocity

To show the validity of the simulation results, particle velocity components are compared with the measured data by Zabrodiec et al. [29] using laser Doppler velocimetry (see the dotted red lines compared

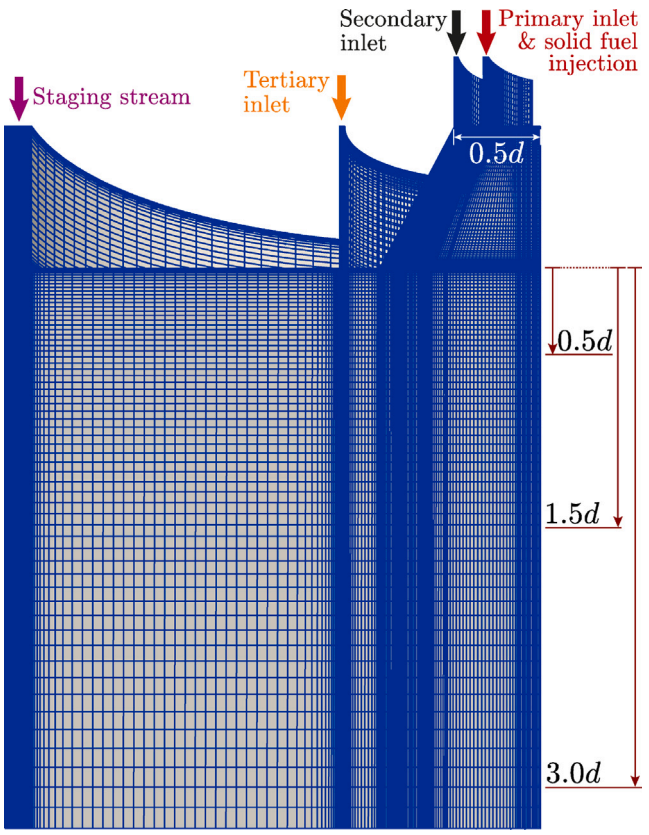

Fig. 3. Structured mesh of the simplified geometry of the combustion chamber used in the numerical simulations. The distances specified with d under the dump plane (diffuser outlet) mark the positions for which the results of the different cases are compared to each other.

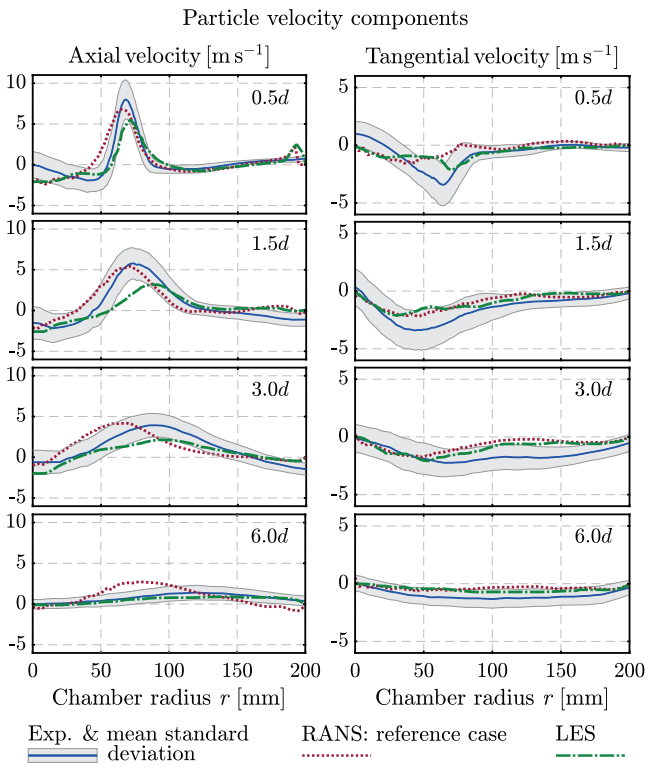

Fig. 4. Validation of the numerical simulations by comparing the cell-averaged axial and tangential particle velocity components with experimental data [29] and LES results [39]. (For interpretation of the references to colour in this figure legend, the reader is referred to the web version of this article.)

to the blue lines in Fig. 4). These results are also compared with the LES results by Nicolai et al. [39] (dotted green lines in Fig. 4). The comparisons show good agreement with both measurements and LES results. Therefore, verification and validation studies both indicate the eligibility of the coarser grid for further simulations.

Particle temperature

In addition to the velocity components, particle temperature obtained from the simulation of the reference case is compared with the measurements [58] and the LES results [39] on different distances (levels) in the chamber over the chamber radius (see Fig. 5). Measurement of particle temperature has been based on the collected flame radiation and fitting it to the Planck black body radiation. The flame radiation was collected by (1) a non-intrusive narrow-angle optical system providing integrated line-of-sight radiation data, and (2) an intrusive cold-background optical probe that collects radiation from integrated line-of-sight radiation within a reduced measurement volume [58].

Despite the good agreement in the velocity comparison, the simulation results for the particle temperature tend to overestimate the experimental results in a radial range $r < 100$ mm. However, the results of the RANS simulation agree well with those of the LES, except for the deviations at a level of 100 mm (1.5625d) below the dump plane. This can be attributed to the detailed gas-phase chemistry used in the LES compared to the two-reaction mechanism used in this study (see Section 3.1.2). Deviations with measured particle temperatures in such a range were also reported in other similar studies, not only in the RANS simulations [33,59,60], but also in the high-fidelity LES [34,39,59,60]. Such deviations with particle temperature measurements can be due to both numerical and experimental uncertainties: (1) in particular, difference between the measurement volume and the corresponding cell

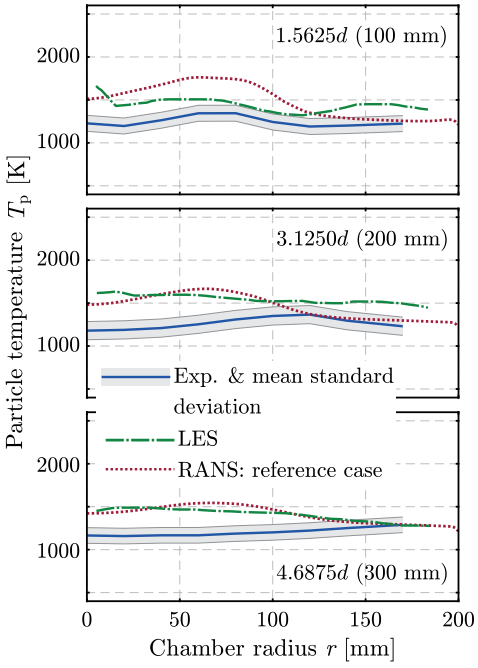

Fig. 5. Validation of the RANS simulation results for cell-averaged particle temperature in comparison to the experimental data by Zabrodiec et al. [58] and LES data by Nicolai et al. [39]. Comparisons were made on different levels in the combustion chambers specified by the outer diameter of the secondary inlet d.

Table 4
Gas and particle radiative properties applied in radiation transfer equation (5) for various simulation cases.

Scenario	κ_g	κ_p	σ_p	$Q_{abs,p}$	$Q_{sca,p}$
Only gas radiation	WSGG[b]	0	0	0	0
Reference case[a]	WSGG[b]	Eq. (8)	Eq. (10)	0.9	0.01
Mie	WSGG[b]	Eq. (8)	Eq. (10)	Eq. (12a) & Fig. 2	Eq. (12b) & Fig. 2
WSA	WSGG[b]	Eq. (13a)	Eq. (13b)	Eq. (12a) & Fig. 2	Eq. (12b) & Fig. 2

[a] The particle radiative properties are considered constant according to parameters such as wavelength, temperature, burnout degree, and particle diameter.
[b] Modified WSGGM according to Bordbar et al. [11].

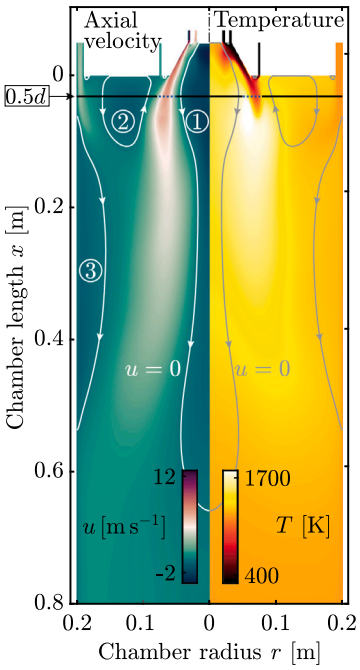

Fig. 6. Axial velocity u and temperature T fields of the gas phase with the stagnation contour line of the axial velocity ($u = 0$) on both fields. The horizontal black line indicates a level of $0.5d$ below the dump plane, where $d = 64$ mm is the outer diameter of the secondary inlet. The blue dotted line portion on this black line specifies the approximate section through which the secondary flow passes. (For interpretation of the references to colour in this figure legend, the reader is referred to the web version of this article.)

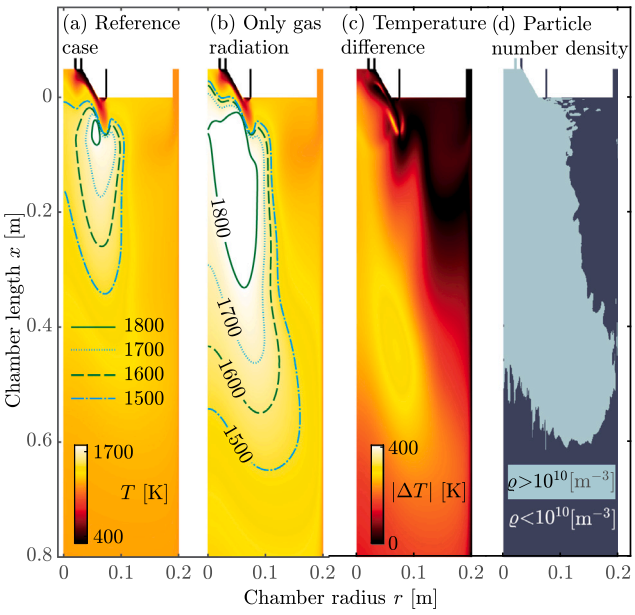

Fig. 7. Influence of the particle radiation on the gas temperature field: (a) gas temperature field obtained for the reference case, (b) gas temperature field obtained by considering only gas radiation, (c) absolute temperature difference between the two cases, and (d) particle number density distribution ϱ for the reference case. (For interpretation of the references to colour in this figure legend, the reader is referred to the web version of this article.)

volume of the numerical grid at the respective measurement point; (2) RANS simulations may not be able to completely render the turbulent nature of the swirl flame; and (3) sensitivity of the flame to the kinetic parameters for devolatilisation and char burnout, i.e., the kinetic rates influence the flame structure leading to changes in the temperature field [61]. Therefore, accurate particle reaction kinetics and a more precise devolatilisation model, such as a two-step model, can reduce the discrepancies.

A detailed discussion on the possible reasons for discrepancies with the temperature measurements has also been given by Nicolai et al. [39]. The important point for the RANS simulations in this study is using a verified model to assess the level of detail needed for modelling particle radiation in the simulation. The minimum required level can then be used in the high-fidelity simulations.

5.2. Flame characterisation: axial velocity and temperature

Here, the reference case is characterised concerning the axial velocity and the temperature fields. The employed radiation properties for this case are summarised in Table 4. Fig. 6 shows that the axial velocity field of the reference case exhibits three recirculation zones (RZ): ①the inner RZ around the axis of the chamber extending from the diffuser to $x \approx 0.64$ m, ②the external RZ between the tertiary inlet and the staging stream, and ③the wall RZ below the staging stream. The temperature field indicates the particle heat-up region (transition from red to yellow in the burner region/diffuser) accompanied by the reaction region (the yellow and white region). The heat generated through the reaction is transported downward and is partly brought back to the diffuser via the inner RZ. In this way, the inner RZ contributes to the stabilisation of the flame [29,33,62,63].

5.3. Role of the gas radiation and particle radiation interaction

In this section, the importance of gas radiation and particle radiation in the formation of the flame is studied. This is carried out by neglecting the contribution of particle radiation in the heat transfer mechanism in the reference case. The relevant radiative properties for both simulation cases (reference and only gas radiation) can be taken from Table 4. The resulting gas temperature field is compared to that of the reference case in Fig. 7. The temperature field of the reference case (Fig. 7(a)) exhibits lower temperatures than that of Fig. 7(b) for the case without particle radiation.

The difference between the obtained temperature fields (see Fig. 7(c)) emphasises the overriding importance of particle radiation on flame temperatures. Neglecting the role of particle radiation in the heat transfer leads to higher flame temperatures both in the near-burner region and further downstream because the produced energy by the combustion process is not absorbed by the particles, resulting in higher gas temperatures. In other words, more energy is available to

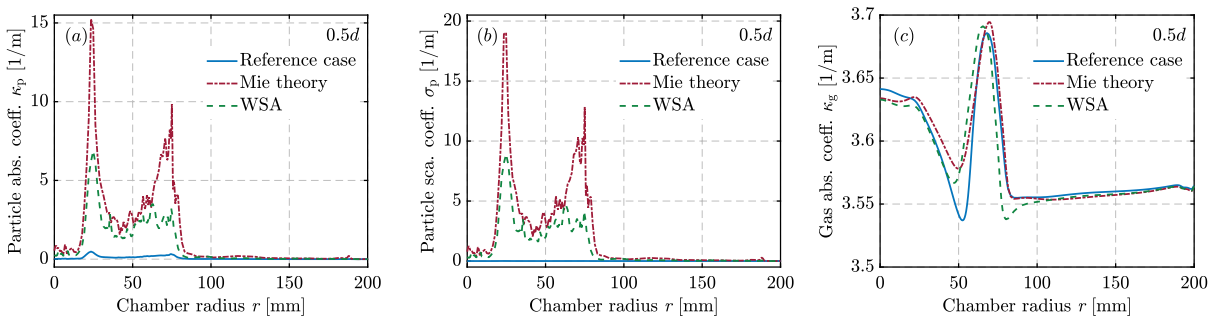

Fig. 8. Comparison of the (a) particle absorption, (b) particle scattering, and (c) gas absorption coefficients over the radius of the chamber on a distance of $0.5d$ below the dump plane obtained for three cases investigated: (1) Reference case, (2) Mie, (3) WSA.

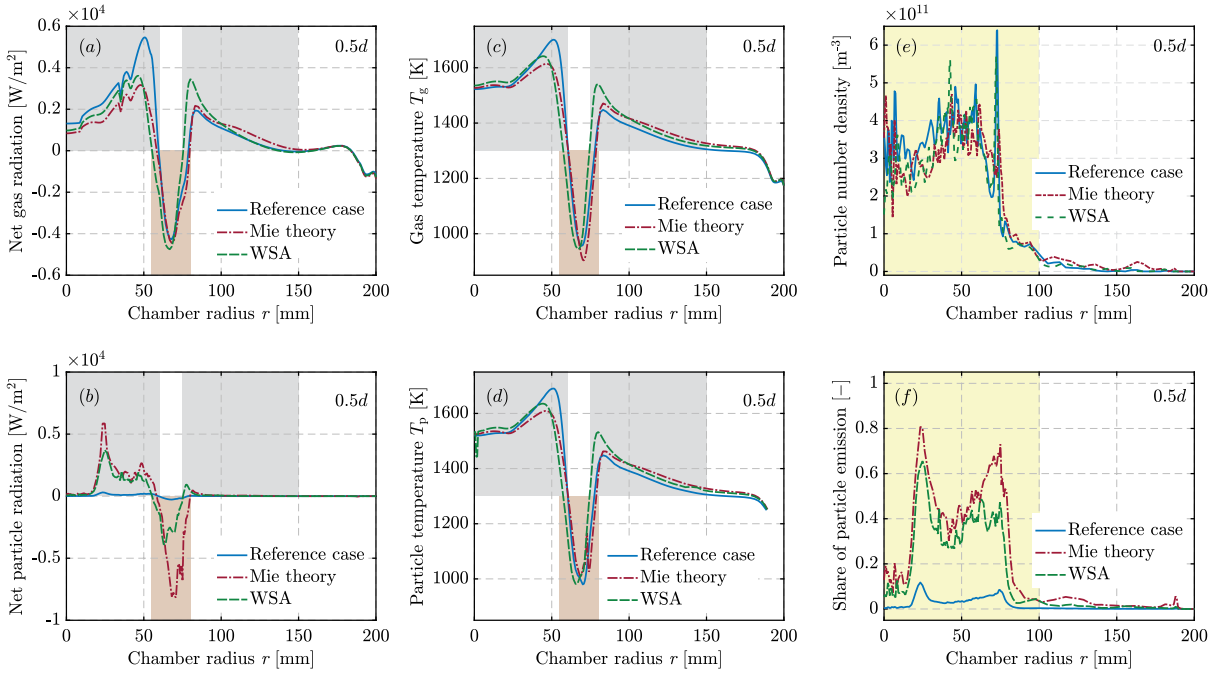

Fig. 9. Evaluation of the net gas (a) and particle (b) radiation, gas (c) and particle (d) temperatures, particle number density (e), and proportion of particle emission (f) using Eq. (16) along the cell length (s) and over all directions at a distance of $0.5d$ below the dump plane in (1) Reference case, (2) Mie theory, and (3) WSA. Grey zones indicate the radial ranges, where emission dominates absorption. In the orange zones, absorption dominates emission. The yellow zone depicts the radial range, where particle effects are important in the radiation exchange. (For interpretation of the references to colour in this figure legend, the reader is referred to the web version of this article.)

be absorbed by the gas. This is more pronounced in the regions with a high particle number density when comparing Figs. 7(c) and 7(d).

5.4. Assessment of the level of detail in particle radiation modelling

Fig. 7 emphasises the importance of the particle radiation on the flame characteristics. In this section, the level of detail in modelling particle radiation is investigated. Accordingly, the more detailed methods available in the literature for the calculation of the particle radiative properties are considered in the simulation: the Mie case and the WSA case. Table 4 provides an overview of the differences in the calculation of the radiation properties in the simulations.

In the Mie case, the burnout-dependency of particle radiative properties is considered and in the WSA case, the influence of non-uniformity in the distribution of particles within a computational cell on the burnout-dependent particle radiative properties is additionally taken into account. According to Eqs. (8) and (10), the absorption and scattering coefficients are the direct variables that can be affected by the particle radiative properties. In the following, these quantities are evaluated and then different terms of the radiation transfer equation containing the absorption and scattering coefficients are investigated.

5.4.1. Particle absorption and scattering coefficients

Figs. 8(a) and 8(b) present the influence of the burnout-dependent particle radiative properties without and with considering the influence of the cellwise non-uniform particle distribution on the particle absorption and scattering coefficients using the WSA. The particle absorption coefficients in the Mie and WSA cases are significantly higher than in the reference case (see Fig. 8(a)). The obtained particle scattering coefficients within the Mie and WSA cases are even higher than their absorption coefficients (Fig. 8(b)). This is following the observations by Koch et al. [28].

Fig. 8(c) shows the calculated gas absorption coefficients for the three cases. Differences in the gas absorption coefficients in Fig. 8(c) are not a direct consequence of the changed particle absorption and scattering coefficients, since the gas absorption coefficient depends only on the gas temperature and composition (see Eqs. (6a) and (6b)). However, variation of the radiative properties of the particles with temperature and diameter (burnout-dependent properties with or without the inclusion of non-uniformity effects using the WSA) indirectly changes the gas temperature and concentration fields due to interactions (e.g. convective heat transfer).

5.4.2. Evaluation of the radiation transfer equation

In order to better distinguish the role of particle and gas radiation in the flame characteristics of the simulation cases introduced in Table 4, the radiative transfer equation, Eq. (5), is analysed in detail in this section.

Multiplying the radiation transfer equation with $\mathrm{d}s$ and $\mathrm{d}\Omega$ and then integrating both sides leads to the following expression:

$$\begin{aligned}\int_0^{4\pi}\int_0^{s} \mathrm{d}I\left(\vec{r},\vec{s}\right)\mathrm{d}\Omega &= \int_0^{s}\int_0^{4\pi} \kappa_{\mathrm{g}} n^2 \frac{\sigma T^4}{\pi}\,\mathrm{d}\Omega\,\mathrm{d}s \\ &+ \int_0^{s}\int_0^{4\pi} \lim_{V\longrightarrow 0}\sum_{\mathrm{n}=0}^{\mathrm{N}} \varepsilon_{\mathrm{pn}} A_{\mathrm{pn}} \frac{\sigma T_{\mathrm{pn}}^4}{\pi V}\,\mathrm{d}\Omega\,\mathrm{d}s \\ &- \int_0^{s}\int_0^{4\pi} \left(\kappa_{\mathrm{g}}+\kappa_{\mathrm{p}}+\sigma_{\mathrm{p}}\right) I\left(\vec{r},\vec{s}\right)\mathrm{d}\Omega\,\mathrm{d}s \\ &+ \int_0^{s}\int_0^{4\pi} \frac{\sigma_{\mathrm{p}}}{4\pi}\int_0^{4\pi} I\left(\vec{r},\vec{s}\prime\right)\Phi\left(\vec{r},\vec{s}\right)\mathrm{d}\Omega\,\mathrm{d}\Omega\,\mathrm{d}s\end{aligned} \tag{15}$$

Since the gas and particle temperatures (T and T_{pn}), gas and particle absorption coefficients κ_{g} and κ_{p}, and particle scattering coefficient σ_{p} are known for a simulated case and taking advantage of the definition of incident radiation $G = \int_{4\pi} I\left(\vec{r},\vec{s}\right)\mathrm{d}\Omega$ (see Eq. (1c)), Eq. (15) can be rewritten as follows:

$$\begin{aligned}G = \underbrace{\overbrace{4s\kappa_{\mathrm{g}} n^2\sigma T^4}^{\text{emission}} - \overbrace{\kappa_{\mathrm{g}} G s}^{\text{absorption}}}_{\text{net gas radiation}} &+ \underbrace{\overbrace{4s\lim_{V\longrightarrow 0}\sum_{\mathrm{n}=0}^{\mathrm{N}}\varepsilon_{\mathrm{pn}}A_{\mathrm{pn}}\frac{\sigma T_{\mathrm{pn}}^4}{V}}^{\text{emission}} - \overbrace{\kappa_{\mathrm{p}} G s}^{\text{absorption}}}_{\text{net particle radiation}} \\ &+ \underbrace{\int_0^{4\pi}\int_0^{s}\frac{\sigma_{\mathrm{p}}}{4\pi}\int_0^{4\pi} I\left(\vec{r},\vec{s}\prime\right)\Phi\left(\vec{r},\vec{s}\right)\mathrm{d}\Omega\,\mathrm{d}\Omega\,\mathrm{d}s}_{\text{inscattering}} - \underbrace{\sigma_{\mathrm{p}} G s}_{\text{outscattering}}\end{aligned} \tag{16}$$

Eq. (16) can be used to evaluate the net contribution of the gas and particle phases in radiation exchange. This is done in Fig. 9. To better describe the changes in the variables, an inner ($r \leq 100$ mm) and an outer ($r > 100$ mm) radial region is defined.

Figs. 9(a) and 9(b) show the net contribution of the gas and particle phases in the radiation exchange, respectively. The net radiation exchange has been obtained by subtracting the absorbed from the emitted amount of radiation in each cell for both phases. The positive values in Figs. 9(a) and 9(b) show higher amounts of emission than absorption and the negative values vice versa. In both phases, the troughs of the profiles in the inner radial region indicate the influence of the strong secondary flow on the net radiation exchange. This strong secondary flow induces a transition from the positive (grey zone) to negative (orange zone) values around $r = 50$ mm. A back transition to positive values happens around $r = 80$ mm, which is the end of the width of the secondary flow (see the blue dotted section on the 0.5 level in Fig. 6 as well).

In these positive and negative zones, the three cases (reference, Mie, and WSA) can now be compared concerning the gas (Fig. 9(c)) and particle (Fig. 9(d)) temperatures. The net gas radiation behaves very similarly to the gas temperature, although the reaction enthalpy of the gas phase reactions and the convective exchange between gas and particles also affect the temperature. However, a comparison of Mie and WSA cases shows that the gas temperature is higher if a case has a higher positive value for the net gas radiation. Such a comparison cannot be made with the reference case. For instance, in the radial range $r < 20$ mm, a higher net gas radiation is observed in the reference case than in the other cases, but the gas temperature in this range is not higher in the reference. The reason can be attributed to the gas absorption coefficient obtained in this case (see Fig. 8(c)). Indeed, neglecting the detailed modelling of the particle radiative properties leads to considerable local changes in the temperature of the flame (especially in the regions with high temperature gradients) and this eventually results in the differences in the gas absorption coefficient and vice versa.

Neglecting the more detailed modelling of the particle radiative properties in the reference case significantly underestimates the net particle radiation shown in Fig. 9(b) compared to the other cases. The underestimation is about 18% and 11% difference when comparing the crests of the curves in the first emitting zone (first grey zone) and about 28% and 14% when comparing in the absorbing zone. Since the particles themselves are a heat source, higher absorption coefficients facilitate better interaction between gas and particles such that local temperature peaks are more likely to be avoided. However, due to the complexity of the system and the diverse interactions, a single effect cannot directly be described by a specific modelling. In comparison with the WSA and Mie cases, significantly higher local particle temperatures, e.g., about 300 K and 200 K at $r = 55$ mm, are observed in the reference case. This is due to the strong local temperature gradients meaning that small radial displacements can accordingly lead to large differences between the cases at the same radial position.

Figs. 9(e) provide the particle number densities in the inner (coloured yellow) and outer radial regions. This means that, in the inner radial region, particle radiation can be more important than gas radiation and in the outer radial region vice versa. To prove this, Fig. 9(f) is shown. Except for the reference case, the other two cases confirm the strong increase in the importance of particle radiation in the inner radial region, while gas radiation dominates in the outer region. The influence of the secondary flow on the change in the importance of the particle and gas radiation is also nicely shown with the double peaks. Indeed, the importance of gas emission in the secondary stream becomes higher than the particle emission for the Mie and WSA cases. The reason for the second radial peak is the external recirculation zone (see also Fig. 6), which rotates counter-clockwise and directly after the secondary stream in the radial direction has an opposite direction to the secondary stream. This leads to an increase in the particle number density. Note that although the particle number density is high in the inner radial region for all three cases, the predicted share of particle emission is significantly underestimated in the reference case.

5.4.3. Comparison with experimental results

This section investigates whether the new modelling approaches lead to a better description of the experimental data. Since deviations between the numerical and experimental results for the particle temperatures observed in Fig. 5 were higher than those of the velocity in Fig. 4, the particle temperatures are compared in Fig. 10 once again with the newly obtained predictions using the Mie approach and the WSA at the axial distances $1.5625d$, $3.1250d$, and $4.6875d$. Although high local temperature differences of about 300 K and 200 K (see Fig. 9(d)) at an axial distance of $0.5d$ exist in the predictions of the reference case compared to the WSA and Mie cases, respectively, Fig. 10 shows that the differences between the cases themselves are small compared to the differences each case has to the measurements. Thus, in comparison with the measurements, no significant improvement is achieved. Since the experimental data are available relatively far away from the near-burner region, the role of particle radiation can be less pronounced at the comparison levels. This said, the results show that when temperatures far away of the burner are of interest, using complex models for particle radiative properties is not decisive.

To prove the level of importance of the role of particle radiation at different axial distances, Fig. 11 is provided for the WSA case. This figure shows that the importance of particle radiation is partly more than 60% at the levels above $0.5d$. Inside the diffuser (negative distances) or at the dump plane ($x = 0$), this share is even above 80%. However, for the highest level, at which the experimental data are available ($1.5625d$), the role of particle radiation decreases below 20%. This can be the reason for the small improvement in the comparison of the temperature profiles against the experimental data.

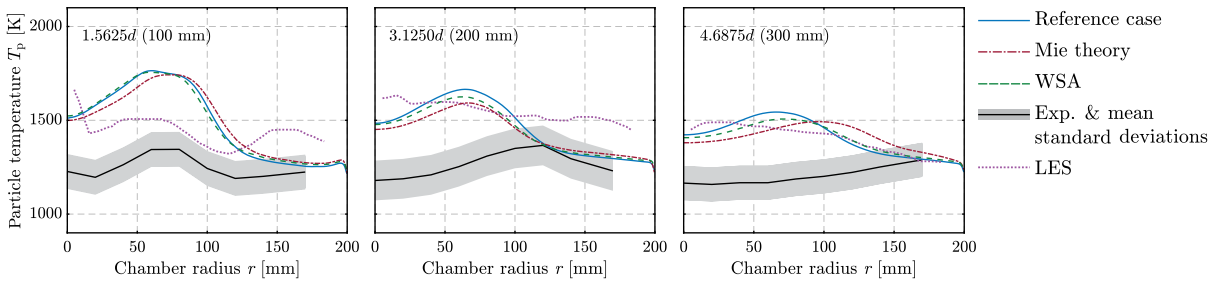

Fig. 10. Comparison of the particle temperature obtained in different cases (Reference case, Mie theory, and WSA) with the measurements on different axial distances over the radius of the chamber.

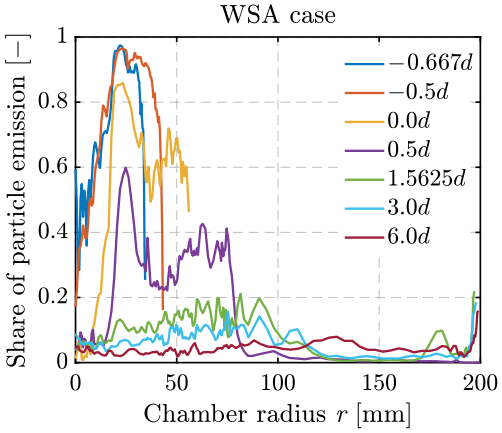

Fig. 11. Proportion of particle emission at different axial levels in the chamber obtained in the WSA case.

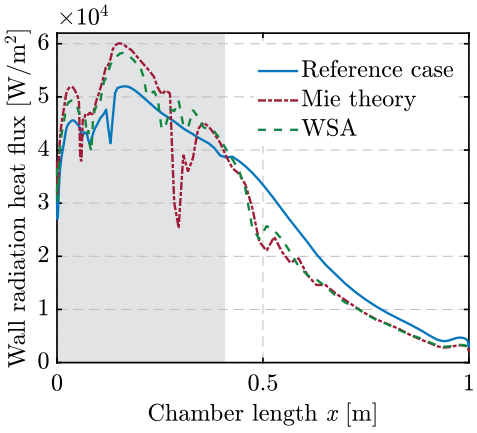

Fig. 12. Comparison of the wall radiative heat flux obtained in different cases (Reference case, Mie theory, and WSA).

5.4.4. *Wall radiation heat flux*

The influence of different approaches on the net radiation heat fluxes on the chamber wall is shown in Fig. 12, signifying considerable local differences. These local differences can be attributed to the changes in the particle number densities. For instance, in an axial range of $0.277 < x < 0.340$ mm, the sudden decrease in the wall radiation heat flux for the Mie case is due to the sudden local increase in the particle number density by approximately up to 35% compared to the other cases. In most part of the upstream region ($x < 0.4$ m), the reference case leads to lower wall radiation heat fluxes compared to the other two cases, while in the downstream region, higher wall radiative heat fluxes are observed for the reference case. This can also be attributed to the importance of particle radiation in the upstream region of the chamber (see Fig. 11) and consequently higher wall radiation heat fluxes in the Mie and WSA cases. In the downstream region, where the importance of particle radiation decreases, the predictions of all three cases converge.

6. Conclusion

This study aimed to develop a simulation tool for investigating the role of particle-radiation interactions in the combustion of pulverised solid fuels under oxyfuel conditions. For this purpose, a reference case, Oxy25 flame (25 vol% O_2 and 75 vol% CO_2), was chosen from the cases measured by Zabrodiec et al. [29,58]. A simulation of the reference case was carried out with the aid of a developed simulation tool in Ansys Fluent by adopting the submodels for oxyfuel conditions via user-defined functions. This included models for particle reaction kinetics as well as gas and particle radiative properties. Gas radiative properties were modelled implementing a modified weighted-sum-of-grey-gases model. Particle radiative properties were modelled implementing tabulated data that include burnout-dependent absorption and scattering efficiencies for both char and ash particles. These tabulated data were pre-calculated using the Mie theory. During the simulation, ash and char absorption and scattering efficiencies were interpolated for their current diameter and temperature. In this way, a recently proposed weighted-scaling approach by Koch et al. [28], which accounts for the effects of non-uniformity of particle distribution in computational cells on the burnout-dependent particle radiative properties, was considered in the simulations that should lead to a more realistic case. The simulation results concerning the overall gas temperature fields, the local temperature profiles, the radiation transfer equation, absorption and scattering coefficients, and the wall radiation heat fluxes were investigated. First, the importance of radiation modelling in the chamber was studied by systematically neglecting particle radiation in the solution of the radiation heat transfer equation. The results indicated the significant role of particle radiation in the near-burner region. Second, the radiation transfer equation (RTE) was studied concerning the individual terms in the equation for three different cases: (1) the reference case with constant particle radiative properties; (2) the Mie case with burnout-dependent particle radiative properties; and (3) the WSA case considering weighted-scaling approach to account for the influence of cellwise non-uniform particle distribution on the burnout-dependent particle radiative properties. The evaluated results close to the burner over the radius showed:

1. significant changes in the absorption and scattering coefficients;
2. two radial regions with high (the inner region) and low (the outer region) particle number densities;
3. in the inner region, the influence of particle radiation on the radiation fluxes was in the Mie and WSA cases significant, while in the outer region gas radiation was dominating (for all three cases); and
4. at the radial positions with high temperature gradients, significant local temperature differences about 200 – 300 K;

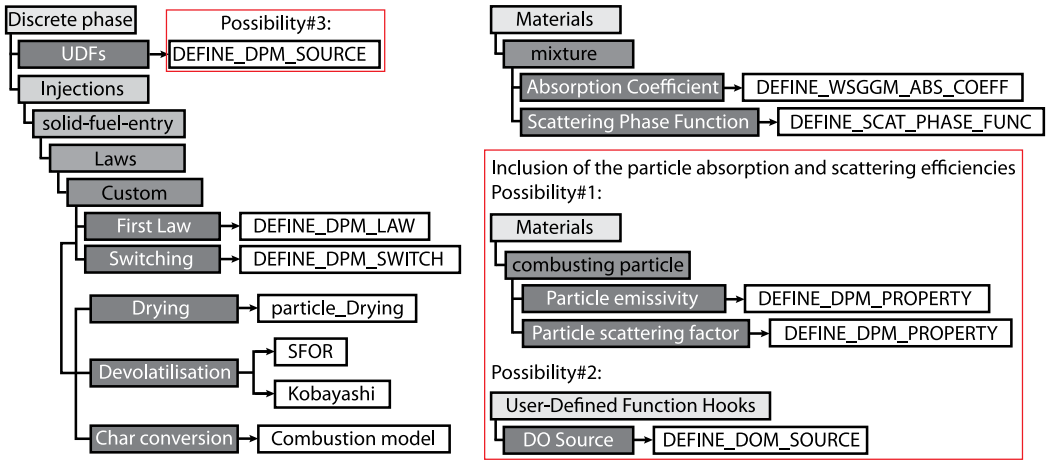

Fig. 13. General scheme of the structure of the compiled user-defined functions in the code including the possible interfaces to consider modifications for particle radiative properties. (For interpretation of the references to colour in this figure legend, the reader is referred to the web version of this article.)

Comparisons of the results obtained using a more detailed modelling of particle radiative properties with temperature measurements did not lead to significant improvements since the available experimental data are for the axial distances relatively far away from the burner, where the role of particle radiation significantly reduces compared to the near-burner region. The results on the wall radiative heat flux signified an upstream $x < 0.4$ m and a downstream region. In the upstream region, the reference case led to smaller wall radiative heat fluxes compared to the other cases. This was attributed to the underestimation of the particle radiative heat fluxes in the reference case. The differences between the results of the Mie and WSA on the wall radiative heat fluxes cases were overall small and in the downstream region $x \geq 0.4$, predictions of both models converged. Note that in a real combustion chamber, the operating conditions are different and temperatures are significantly higher than in the pilot-scale chamber investigated in this study. These can affect the importance of particle radiation by local changes in particle number densities.

CRediT authorship contribution statement

Hossein Askarizadeh: Writing – review & editing, Writing – original draft, Validation, Software, Resources, Methodology, Investigation, Formal analysis, Data curation, Conceptualization. **Stefan Pielsticker:** Writing – review & editing, Supervision, Conceptualization. **Hendrik Nicolai:** Writing – review & editing, Validation, Supervision, Data curation, Conceptualization. **Matthias Koch:** Writing – review & editing, Data curation, Conceptualization. **Reinhold Kneer:** Writing – review & editing, Supervision, Project administration, Funding acquisition. **Christian Hasse:** Supervision, Project administration. **Anna Maßmeyer:** Writing – review & editing, Supervision, Project administration.

Declaration of competing interest

This manuscript describes original work and is not under consideration by any other journal. All authors approved the manuscript and this submission and have no conflicts of interest to disclose.

Data availability

The data will be published through the library of the RWTH Aachen University as data publication under the DOI: 10.18154/RWTH-2024-07124.

Acknowledgements

This work has been funded by the Deutsche Forschungsgemeinschaft (DFG, German Research Foundation) – 215035359 – SFB/TRR 129 ‘Oxyflame’.

Appendix. Developed code

A detailed description of the developed code via user-defined functions (UDFs) in Ansys Fluent will appear in a Software publication document by the RWTH library under the DOI: 10.18154/RWTH-2024-05749. The developed code calculates particle kinetics, such as inert heating, devolatilisation and char conversion, and particle and gas radiative properties, such as absorption coefficients of gas and particles, scattering coefficient of particles, and also scattering phase function outside of the main Ansys Fluent code.

Fig. 13 provides a general overview where the compiled UDFs in Ansys Fluent are incorporated in the simulation. The red boxes show the possibilities for including the UDFs for particle radiative properties. Note that the shown structure in Fig. 13 does not include all the UDFs available in the code. Many of the UDFs are indirectly involved in the solution procedure.

References

[1] IEA, World Energy Outlook, Paris. 2022, https://www.iea.org/reports/world-energy-outlook-2022.
[2] Hasse C, Debiagi P, Wen X, Hildebrandt K, Vascellari M, Faravelli T. Advanced modeling approaches for CFD simulations of coal combustion and gasification. Prog Energy Combust Sci 2021;86:100938. http://dx.doi.org/10.1016/j.pecs.2021.100938.
[3] Sommariva S, Maffei T, Migliavacca G, Faravelli T, Ranzi E. A predictive multi-step kinetic model of coal devolatilization. Fuel 2010;89(2):318–28. http://dx.doi.org/10.1016/j.fuel.2009.07.023.
[4] Maffei T, Khatami R, Pierucci S, Faravelli T, Ranzi E, Levendis YA. Experimental and modeling study of single coal particle combustion in O_2/N_2 and Oxy-fuel (O_2/CO_2) atmospheres. Combust Flame 2013;160(11):2559–72. http://dx.doi.org/10.1016/j.combustflame.2013.06.002.
[5] Nicolai H. Towards predictive simulations of low-emission reactive solid fuel systems [Ph.D. thesis], Darmstadt: Technische Universität; 2022, http://dx.doi.org/10.26083/tuprints-00021079, xiv, 192 Seiten.
[6] Nicolai H, Debiagi P, Wen X, Dressler L, Maßmeyer A, Janicka J, et al. Flamelet LES of swirl-stabilized oxy-fuel flames using directly coupled multi-step solid fuel kinetics. Combust Flame 2022;241. http://dx.doi.org/10.1016/j.combustflame.2022.112062.
[7] Nicolai H, Debiagi P, Janicka J, Hasse C. Flamelet LES of oxy-fuel swirling flames with different O_2/CO_2 ratios using directly coupled seamless multi-step solid fuel kinetics. Fuel 2023;344:128089. http://dx.doi.org/10.1016/j.fuel.2023.128089.
[8] Badzioch S, Hawksley PG. Kinetics of thermal decomposition of pulverized coal particles. Ind Eng Chem Process Des Develop 1970;9(4):521–30.

[9] Baum M, Street P. Predicting the combustion behaviour of coal particles. Combust Sci Technol 1971;3(5):231–43. http://dx.doi.org/10.1080/00102207108952290.

[10] Field MA, Gill DW, Morgan BB, Hawksley PGW. Combustion of pulverised coal. 1967.

[11] Bordbar MH, Wecel G, Hyppänen T. A line by line based weighted sum of gray gases model for inhomogeneous CO_2–H_2O mixture in oxy-fired combustion. Combust Flame 2014;161(9):2435–45. http://dx.doi.org/10.1016/j.combustflame.2014.03.013.

[12] Kez V, Consalvi J-L, Liu F, Ströhle J, Epple B. Assessment of several gas radiation models for radiative heat transfer calculations in a three-dimensional oxy-fuel furnace under coal-fired conditions. Int J Therm Sci 2017;120:289–302. http://dx.doi.org/10.1016/j.ijthermalsci.2017.06.017.

[13] Modest MF, Mazumder S. Radiative heat transfer. Elsevier Science; 2021.

[14] Smith TF, Shen ZF, Friedman JN. Evaluation of coefficients for the weighted sum of gray gases model. J Heat Transf 1982;104(4):602–8. http://dx.doi.org/10.1115/1.3245174.

[15] Nikolopoulos N, Agraniotis M, Violidakis I, Karampinis E, Nikolopoulos A, Grammelis P, et al. Parametric investigation of a renewable alternative for utilities adopting the co-firing lignite/biomass concept. Fuel 2013;113:873–97. http://dx.doi.org/10.1016/j.fuel.2013.03.034.

[16] Backreedy RI, Fletcher LM, Ma L, Pourkashanian M, Williams A. Modelling pulverised coal combustion using a detailed coal combustion model. Combust Sci Technol 2006;178(4):763–87. http://dx.doi.org/10.1080/00102200500248532.

[17] Al-Abbas AH, Naser J, Dodds D. CFD modelling of air-fired and oxy-fuel combustion of lignite in a 100kW furnace. Fuel 2011;90(5):1778–95. http://dx.doi.org/10.1016/j.fuel.2011.01.014.

[18] Guo J, Liu Z, Huang X, Zhang T, Luo W, Hu F, et al. Experimental and numerical investigations on oxy-coal combustion in a 35 MW large pilot boiler. Fuel 2017;187:315–27. http://dx.doi.org/10.1016/j.fuel.2016.09.070.

[19] Liu ZH, Zheng CG, Xing HW. Radiative properties of residual char and its effects on radiative heat transfer in pulverized coal fired furnaces. Develop Chem Eng Min Process 2000;8(3–4):269–79. http://dx.doi.org/10.1002/apj.5500080307.

[20] Gronarz T, Habermehl M, Kneer R. Modeling of particle radiative properties in coal combustion depending on burnout. Heat Mass Transf 2017;53(4):1225–35. http://dx.doi.org/10.1007/s00231-016-1896-0.

[21] Gronarz T. Modeling of particle-radiation-interaction for the numerical simulation of coal combustion [Ph.D. thesis], Aachen: RWTH Aachen University; 2017, p. 1 Online–Ressource (g, 157 Seiten) : Illustrationen. http://dx.doi.org/10.18154/RWTH-2018-223279.

[22] Lockwood FC, Rizvi SMA, Shah NG. Comparative predictive experience of coal firing. Proc Inst Mech Eng C 1986;200(2):79–87. http://dx.doi.org/10.1243/PIME_PROC_1986_200_100_02.

[23] Yin C. On gas and particle radiation in pulverized fuel combustion furnaces. Appl Energy 2015;157:554–61. http://dx.doi.org/10.1016/j.apenergy.2015.01.142.

[24] Guo J, Hu F, Luo W, Li P, Liu Z. A full spectrum k-distribution based non-gray radiative property model for unburnt char. Proc Combust Inst 2019;37(3):3081–9. http://dx.doi.org/10.1016/j.proci.2018.06.009.

[25] Guo J, Hu F, Jiang X, Li P, Liu Z. Effects of gas and particle radiation on IFRF 2.5 MW swirling flame under oxy-fuel combustion. Fuel 2020;263:116634. http://dx.doi.org/10.1016/j.fuel.2019.116634.

[26] Askarizadeh H, Nicolai H, Zabrodiec D, Pielsticker S, Hasse C, Kneer R, et al. Numerische Untersuchung zur Relevanz von Teilmodellen für Pyrolyse und Koksabbrand in turbulenten drallbehafteten Flammen unter Oxyfuel-Bedingungen. In: 30. Deutscher flammentag, Hannover, Deutschland. 2021, http://dx.doi.org/10.18154/RWTH-2021-10123.

[27] Askarizadeh H, Koch M, Nicolai H, Pielsticker S, Kneer R, Hasse C, et al. Influence of gas radiation, particle radiation interactions, and conversion-dependent particle radiative properties on pulverized solid fuel combustion. In: 31. Deutscher flammentag, Berlin, Germany. 2023, URL https://publications.rwth-aachen.de/record/969879.

[28] Koch M, Pielsticker S, Kneer R. Numerical investigation of the radiative properties of a fully resolved particle cloud. Int J Therm Sci 2023;185:108102. http://dx.doi.org/10.1016/j.ijthermalsci.2022.108102.

[29] Zabrodiec D, Becker L, Hees J, Maßmeyer A, Habermehl M, Hatzfeld O, et al. Detailed analysis of the velocity fields from 60 kW swirl-stabilized coal flames in CO_2/O_2- and N_2/O_2-atmospheres by means of laser Doppler velocimetry and particle image velocimetry. Combust Sci Technol 2017;189(10):1751–75. http://dx.doi.org/10.1080/00102202.2017.1332598.

[30] Chigier NA, Beer JM. Velocity and static-pressure distributions in swirling air jets issuing from annular and divergent nozzles. J Basic Eng 1964;86(4):788–96. http://dx.doi.org/10.1115/1.3655954.

[31] Fluent theory guide 17.1. 2022.

[32] Askarizadeh H, Pielsticker S, Nicolai H, Kneer R, Hasse C, Maßmeyer A. Investigation of the coupling schemes between the discrete and the continuous phase in the numerical simulation of a 60 kW_{th} swirling pulverised solid fuel flame under oxyfuel conditions. Fire 2024;7(6):185. http://dx.doi.org/10.3390/fire7060185.

[33] Toporov D, Bocian P, Heil P, Kellermann A, Stadler H, Tschunko S, et al. Detailed investigation of a pulverized fuel swirl flame in CO_2/O_2 atmosphere. Combust Flame 2008;155(4):605–18. http://dx.doi.org/10.1016/j.combustflame.2008.05.008.

[34] Franchetti BM, Cavallo Marincola F, Navarro-Martinez S, Kempf AM. Large eddy simulation of a 100 kW_{th} swirling oxy-coal furnace. Fuel 2016;181:491–502. http://dx.doi.org/10.1016/j.fuel.2016.05.015.

[35] Magnussen B. On the structure of turbulence and a generalized eddy dissipation concept for chemical reaction in turbulent flow. In: 19th aerospace sciences meeting, St. Louis, Missouri, USA. 1981, p. 42.

[36] Askarizadeh Ravizi H, Nicolai H, Pielsticker S, Kneer R, Hasse C, Maßmeyer AL. Assessment of turbulence modulation for the simulation of a 60-kW_{th} swirling flame of pulverized solid fuel under oxy-fuel conditions. In: 14. International conference on computational heat and mass transfer, Düsseldorf, Germany. 2023, URL https://publications.rwth-aachen.de/record/971272.

[37] Al Taweel AM, Landau J. Turbulence modulation in two-phase jets. Int J Multiphase Flow 1977;3(4):341–51. http://dx.doi.org/10.1016/0301-9322(77)90014-3.

[38] Sadiki A, Agrebi S, Chrigui M, Doost S, Knappstein R, di Mare F, et al. Analyzing the effects of turbulence and multiphase treatments on oxy-coal combustion process predictions using LES and RANS. Chem Eng Sci 2017;166:283–302. http://dx.doi.org/10.1016/j.ces.2017.03.015.

[39] Nicolai H, Wen X, Miranda FC, Zabrodiec D, Maßmeyer A, di Mare F, et al. Numerical investigation of swirl-stabilized pulverized coal flames in air and oxy-fuel atmospheres by means of large eddy simulation coupled with tabulated chemistry. Fuel 2021;287. http://dx.doi.org/10.1016/j.fuel.2020.119429.

[40] Benim AC, Deniz Canal C, Boke YE. A validation study for RANS based modelling of swirling pulverized fuel flames. Energies 2021;14(21). http://dx.doi.org/10.3390/en14217323.

[41] Boyd R, Kent J. Three-dimensional furnace computer modelling. Proc Combust Inst 1988;21(1):265–74. http://dx.doi.org/10.1016/S0082-0784(88)80254-6.

[42] Frössling N. Über die verdunstung fallender Tropfen. Gerlands Beiträge zur Geophysik 1938;52(1):170–216.

[43] Ranz WE. Evaporation from drops-I and-II. Chem Eng Progr 1952;48:141–6.

[44] Jendoubi S, Lee HS, Kim T-K. Discrete ordinates solutions for radiatively participating media in a cylindrical enclosure. J Thermophys Heat Transf 1993;7(2):213–9. http://dx.doi.org/10.2514/3.409.

[45] Kim T-K, Lee HS. Radiative transfer in two-dimensional anisotropic scattering media with collimated incidence. J Quant Spectrosc Radiat Transf 1989;42(3):225–38. http://dx.doi.org/10.1016/0022-4073(89)90086-1.

[46] Boulet P, Collin A, Consalvi JL. On the finite volume method and the discrete ordinates method regarding radiative heat transfer in acute forward anisotropic scattering media. J Quant Spectrosc Radiat Transf 2007;104(3):460–73. http://dx.doi.org/10.1016/j.jqsrt.2006.09.010.

[47] Maxwell J. VIII. A dynamical theory of the electromagnetic field. Philos Trans R Soc London 1865;(155):459–512. http://dx.doi.org/10.1098/rstl.1865.0008.

[48] Draine B, Flatau P. Discrete-dipole approximation for scattering calculations. J Opt Soc Am A 1994;11:1491–9. http://dx.doi.org/10.1364/JOSAA.11.001491.

[49] Mishchenko M, Travis L, Mackowski D. T-matrix computations of light scattering by nonsperical particles: A review. J Quant Spectrosc Radiat Transf 1996;55:535–75. http://dx.doi.org/10.1016/0022-4073(96)00002-7.

[50] Mie G. Beiträge zur Optik trüber Medien, speziell kolloidaler Metallösungen. Ann Phys 1908;330(3):377–445. http://dx.doi.org/10.1002/andp.19083300302.

[51] Gronarz T, Schnell M, Siewert C, Schneiders L, Schröder W, Kneer R. Comparison of scattering behaviour for spherical and non-spherical particles in pulverized coal combustion. Int J Therm Sci 2017;111:116–28. http://dx.doi.org/10.1016/j.ijthermalsci.2016.08.014.

[52] Gronarz T, Hoeges C, Kez V, Habermehl M, Kneer R. Comparison of scattering behaviour for inhomogeneous particles in pulverized coal combustion. Int J Therm Sci 2019;140:1–7. http://dx.doi.org/10.1016/j.ijthermalsci.2019.02.034.

[53] Manickavasagam S, Menguc M. Effective optical properties of pulverized coal particles determined from FT-IR spectrometer experiments. Energy fuels 1993;7(6):860–9. http://dx.doi.org/10.1021/ef00042a023.

[54] Goodwin D, Mitchner M. Flyash radiative properties and effects on radiative heat transfer in coal-fired systems. Int J Heat Mass Transf 1989;32(4):627–38. http://dx.doi.org/10.1016/0017-9310(89)90211-1.

[55] Bohren C, Huffman D. Absorption and scattering of light by small particles. In: Wiley science series, Wiley; 2008.

[56] Mätzler C. MATLAB functions for Mie scattering and absorption, version 2. Institute of Applied Physics, University of Bern; 2002.

[57] Koch M, Pielsticker S, Tarlinski D, Scherer V, Kneer R. Coupling radiative properties with detailed char conversion kinetics. Fuel 2024;363:130973. http://dx.doi.org/10.1016/j.fuel.2024.130973.

[58] Zabrodiec D, Hees J, Maßmeyer A, vom Lehn F, Habermehl M, Hatzfeld O, et al. Experimental investigation of pulverized coal flames in CO_2/O_2- and N_2/O_2-atmospheres: Comparison of solid particle radiative characteristics. Fuel 2017;201:136–47. http://dx.doi.org/10.1016/j.fuel.2016.11.097.

[59] Chen L, Ghoniem AF. Simulation of oxy-coal combustion in a 100 kW_{th} test facility using RANS and LES: A validation study. Energy & Fuels 2012;26(8):4783–98. http://dx.doi.org/10.1021/ef3006993.

[60] Warzecha P, Boguslawski A. LES and RANS modeling of pulverized coal combustion in swirl burner for air and oxy-combustion technologies. Energy 2014;66:732–43. http://dx.doi.org/10.1016/j.energy.2013.12.015.

[61] Askarizadeh H, Pielsticker S, Nicolai H, Kneer R, Hasse C, Özer B, et al. Numerical study on the influence of devolatilisation kinetics on pulverised solid fuel turbulent swirling flames under oxyfuel conditions. In: 14th European conference on industrial furnaces and boilers, Algarve, Portugal. 2024.

[62] Axt C, Maßmeyer A, Pielsticker S, Kneer R. Spatially-resolved experimental investigations of combustion characteristics in a solid fuel doped methane swirl flame and the influence on the formation of ultrafine particulate matter. Combust Flame 2022;244. http://dx.doi.org/10.1016/j.combustflame.2022.112223.

[63] Axt C, Askarizadeh H, Pielsticker S, Kneer R, Maßmeyer A. Investigation of ultrafine particulate matter formation during combustion of biomass and lignite. Energy Fuels 2023;37(1):635–43. http://dx.doi.org/10.1021/acs.energyfuels.2c03278.